Acta Astronautica 172 (2020) 134–139

Contents lists available at ScienceDirect

Acta Astronautica

journal homepage: www.elsevier.com/locate/actaastro

Research paper

Analysis of shock-wave diffraction over double concave cylindrical wedges. Part I: Shock dynamics

N. Brahmi[a,*], A. Hadjadj[a], V. Soni[a], A. Chaudhuri[b]

[a] Normandie University, INSA of Rouen, CNRS, CORIA, 76000 Rouen, France
[b] Department of Civil Engineering and Energy Technology, OsloMet – Oslo Metropolitan University, Pilestredet 35, PB 4, St. Olavs Plass, 0130, Oslo, Norway

ARTICLE INFO

Keywords:
Shock diffraction
Shock waves
Shock reflection
Numerical simulation

ABSTRACT

Shock-wave diffraction over double concave cylindrical surfaces has been numerically investigated at different flow regimes by varying the incident-shock-wave Mach number from $M_s = 1.6$ (transonic) to $M_s = 4.5$ (supersonic regime). The purpose of this study is to better understand the dynamics of shock-wave structure and the associated wave configurations. A mesh-independent solution is obtained and the flow is assessed through different physical quantities (transition angles, triple points trajectories, wall-pressure and skin-friction distributions, velocity and shock location). It is found that the transition angles, from regular to Mach reflection, increase with the Mach number. This phenomenon remains almost the same over both concave surfaces for weak Mach numbers (up to $M_s = 2.5$) and becomes relatively larger on the second surface for high Mach numbers. In terms of shock dynamics, it is found that by increasing the incident incident-shock-wave Mach number to $M_s = 4.5$, unlike the first reflector, the transition from a single-triple-point (STP) wave configuration to a double-triple-point (DTP) wave configuration and back occurred on the second reflector, indicating that the flow is capable of retaining the memory of the past events over the entire process. For the shock velocity, the velocity deficit is found to be increasing with increase in M_s. A best fitting scaling law is derived, to ensure a universal decay of the shock velocity depending on the flow parameters.

1. Introduction

The interaction of shock-waves with rigid boundaries has been the subject of many investigations, since shock-wave diffraction occurs and takes place in the majority of important applications today, such as design of inflow/outflow valves in an internal combustion engine and aerospace propulsion systems. In order to understand the different phenomena resulting from these interactions such as shock-diffraction, shock-reflection, shock-focusing, shock-attenuation and the different flow structures generated by the passage of the shock-wave, several studies have been conducted (Whitham (1956) [1], Whitham (1957) [2], Whitham (1958) [3], Bird (1958) [4], Bazhenova (1978) [5], Henderson (1980) [6], Hilier (1991) [7], Sivier et al. (1992) [8], Skews et al. (2011) [9]). . Two types of shock-reflection configuration namely RR (regular reflection involving two shock waves configuration) and MR (Mach reflection involving three shock waves configuration) were first introduced by the pioneering experimental work of Ernest Mach (1878). However, no significant progress was made until the eminent work of von Neumann in the 1940s. Since then, a considerable amount of work has been carried out in order to better understand the phenomena of shock-waves reflection (Bryson and Gross [10]; Henderson and Lozzi [11]; Krassovskaya and Berezkina [12]; Soni et al. [13]; Chernyshov and Tolpegin [14]). Berezkina et al. were interested in the diffraction of shock waves by cylindrical surfaces. In a first study [23], they studied diffraction of a two-shock configuration by a convex cylindrical surface with the diffraction angle varying continuously, as opposed to [23], where the process, starting at small angles of diffraction, develops at ever-increasing angles, diffraction in [24] starts at a large angle, which progressively decreases. This distinction causes a substantial difference in the formation and development of the structures within the perturbed flow-field. Gvozdeva et al. [15] have found a new pattern of the triple-shock configuration with a negative angle of shock reflection, which is formed in a steady supersonic flow within the range of Mach numbers exceeding 3.0 and specific heat ratios below 1.4. Recently, Smirnov et al. ([16,17]) have investigated mixture ignition and detonation onset in RAM engines due to focusing of a shock wave reflected inside a cone in order to change the mode of flame propagation from slow combustion to detonation. Soni et al. [13] have conducted numerical simulations in order to understand the different wave configurations associated with the shock-wave reflection over

* Corresponding author.
E-mail address: nassim.brahmi@insa-rouen.fr (N. Brahmi).

https://doi.org/10.1016/j.actaastro.2020.01.025
Received 18 February 2019; Received in revised form 31 July 2019; Accepted 17 January 2020
Available online 31 January 2020

double-concave cylindrical reflectors. The double-concave cylinder configuration is different than that presented in Ref. [13] in terms of the orientation and entrance of the shock wave.

In this work, a parametric study is performed to determine the influence of the incident shock strength on shock-wave diffracting mechanism. We use the Navier-Stokes solver to quantify the shock strength, the dynamics of shock-waves and the different wave configurations in shock-wave diffraction over double-concave cylindrical surfaces. Furthermore, different grid resolutions are used to investigate the grid size effect on the results. The paper is organized as follows. Section 2 introduces the numerical methodology used in this study. Section 3 is devoted to introduce the problem set-up and different conditions used in this study. Section 4 is dedicated to discussing the results obtained in this study. In §4.1, the effect of shock strength on transition angle from regular to Mach reflection and triple point trajectories is investigated. The effect of shock strength on shock position and velocity is discussed in §4.2.

2. Governing equations and numerics

2.1. Governing equations

The numerical solution is obtained by solving compressible Navier-Stokes equations for an ideal gas

$$\partial_t \rho + div(\rho \mathbf{v}) = 0 \tag{1}$$

$$\partial_t (\rho \mathbf{v}) + div(\rho \mathbf{v} \otimes \mathbf{v}) + \nabla p = \nabla \tau \tag{2}$$

$$\partial_t (\rho E) + div(\rho E \mathbf{v}) + div(\rho \mathbf{v}) = \nabla(\tau \mathbf{v} + \lambda \nabla T) \tag{3}$$

$$p = (\gamma - 1)\rho e,\ E = \frac{1}{2}\left|\mathbf{v}\right|^2 + e \tag{4}$$

$$\tau = \mu\left[\nabla \otimes \mathbf{v} + (\nabla \otimes \mathbf{v})^T - \frac{2}{3}(\nabla \cdot \mathbf{v})\mathbf{I}\right] \tag{5}$$

where t stands for the time, ρ, $\mathbf{v}$, p, E, T, λ, μ, e are the density, velocity, pressure, total energy, temperature, thermal conductivity, dynamic viscosity and internal energy. The working gas is air with $\gamma = 1.4$ and Prandtl number $Pr = 0.72$. The fluid viscosity follows Sutherland's law.

To simulate the flow field, we used an in-house parallel compressible solver equipped with the adaptive multi-resolution method [18–20]. The code uses an immersed-boundary method (IBM) to handle fluid-solid interaction problems [21]. The solid body is embedded in a Cartesian grid tracked using a ray-tracing technique. Inviscid and viscous fluxes were computed using a fifth-order weighted essentially non-oscillatory (WENO 5) scheme and a fourth-order central difference formula, respectively, while the time was advanced using a third-order Runge-Kutta method [22]. The time step is computed as:

$$\Delta t = \frac{CFL}{max(\Delta t_x, \Delta t_y)} \tag{6}$$

and

$$\Delta t_x = max\left(\frac{|u| + c}{\Delta x}, \frac{2}{\Delta x^2}\frac{\mu}{\rho . Pr}\right) \tag{7}$$

The computations are performed with a CFL number of 0.7, which gives $\Delta t \approx 10^{-8} s$.

3. Problem set-up

Numerical simulations were conducted to understand the dynamics of shock-wave undergoing a double-concave cylindrical surfaces, a schematic representation of the solid is given in Fig. 1. As for the computational specifications, the boundary conditions were set to inlet and outlet at the left (with $\bar{h}$) and the right (with $\bar{H}$) (see Fig. 1), of the computational domain, respectively, while the top boundary and the bottom-right part of the domain are treated as symmetry plane, and the solid surface is considered with a no-slip boundary condition. In all the simulations, the geometric parameters such; $R_1 = R_2 = R = 50\ mm$ and $\omega_1 = \omega_2 = 75°$ were kept constant, the incident Mach number was varied in the range of $1.6 \leq M_s \leq 4.5$. Initially, the shock is located at $x = 5\ mm$ for all Mach numbers. Rankine-Hugoniot relations are used to set the initial conditions for left (shocked state) and right (stagnant state) states associated with the chosen M_s. Air is considered as working fluid and the initial stagnant state is assigned with temperature $T = 300K$ and pressure $p = 101.\ 3kPa$, and the flow is initialized as uniform flow. A grid dependency study is performed to determine the effect of numerics on the results. Grid convergence studies were carried out by using different levels of grid refinement. Five different meshes were used for Mach number $M_s = 1.6$. Table 1 summarizes the relevant parameters for grid sensitivity analysis.

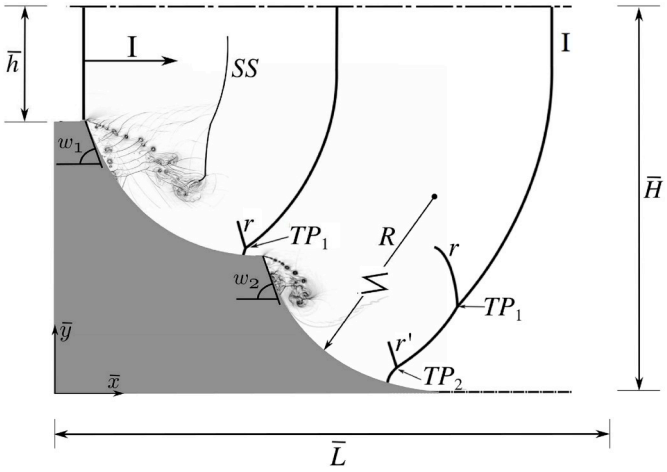

Fig. 1. Schematic representation of a double-concave cylindrical surfaces. *I*: incident shock, *SS*: secondary shock, *r*: reflected shock on the first cylinder, *r'*: reflected shock on the second cylinder, *R*: cylinder surfaces radius, *TP*: triple point, $\bar{h} = 0.32R$, $\bar{H} = 1.8R$, $\bar{L} = 3.4R$, $\bar{x} = x/R$, $\bar{y} = y/R$.

4. Results and discussion

All length scales are normalized by the concave radius $R_1 = R_2 = R = 50\ mm$ and the dimensionless time is defined as $\bar{t} = t.\ a_1/R$ where a_1 is the speed of sound of the gas initially at rest. Fig. 1 shows a planar shock-wave (I) with a Mach number of M_s propagating downstream and diffracting around a corner with a diffracting angle $\omega_1 = \omega_2 = 75°$. When the shock wave arrives on the edge of the first concave, the diffraction process starts. As the diffraction process evolves, the end-wall corner vortices are formed with a rolling-up of eddies that are convected away from the cavity entrance. These corner instabilities are characterized by the formation of a primary vortex that is followed by a secondary one. The key mechanism behind the appearance of this secondary near-wall instability are a large enough advection velocity generated by the cavity boundary layer. It is found that the interaction of this secondary instability with the primary vortex

Table 1
Different grid resolution used, for shock-wave Mach number $M_s = 1.6$ (MP: million points).

Grid	$\Delta x_{min}(\mu m)$	$\Delta y_{min}(\mu m)$	number of points (MP)
$\mathscr{G}_0$	95	88	1.83
$\mathscr{G}_1$	60	50	5.04
$\mathscr{G}_2$	40	40	8.84
$\mathscr{G}_3$	30	29	17.3
$\mathscr{G}_4$	20	21	33.55

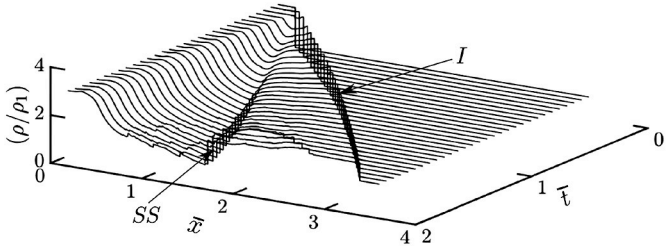

Fig. 2. Evolution of density ratio along $\bar{y} \approx 1.58$ for $M_s = 2.0$, with $\bar{t} = ta_1/R$.

Table 2
Transition angles, from regular to Mach reflection (RR → MR), over the two concave surfaces for different grid resolution for $M_s = 1.6$.

	θ_1^{tr}	θ_2^{tr}
$\mathscr{G}_0$	9. 6°	9. 7°
$\mathscr{G}_1$	10. 7°	10. 8°
$\mathscr{G}_2$	11. 8°	11. 8°
$\mathscr{G}_3$	12. 7°	12. 6°
$\mathscr{G}_4$	12. 7°	12. 6°

core in the upstream part of the cavity is one of the main sources of excitations and possible transition to turbulence and appearance of secondary shocks (*SS*). When the conditions are gathered (the angle between the incident shock wave and the surface of the first concave and the Mach number), reflection of the shock wave takes place and we can see appearance of reflected shocks (*r* for the first concave, *r′* for the second concave) and triple points (TP_1 for the first concave, TP_2 for the second concave), the details of shock reflection are discussed on section 4.1.

Fig. 2 shows density ratio evolution along the axis $\bar{y} \approx 1.58$ for $M_s = 2$, in the space-time diagram. Because of the area increase, the flow and the shock-wave undergo an expansion, the propagation of the incident or primary shock-wave (*I*) in the medium at rest can be clearly observed. Eventually, a left-running (with respect to the fluid) secondary shock-wave (*SS*) appears and is carried to the right because of the supersonic carrier flow.

4.1. Transition angle from regular to Mach reflection

In this section, we present the mesh sensitivity analysis with respect to the transition angle for Regular to Mach reflection (RR → MR). Table 2 shows that the transition angle is the same in both surfaces for all the cases, and it begins to be independent of grid resolution from $\mathscr{G}_3$. Where θ_1^{tr} and θ_2^{tr} are respectively the transition angles in the first and second concave surfaces. Fig. 3 represents non-dimensional wall pressure and skin friction distribution for different grid resolution for

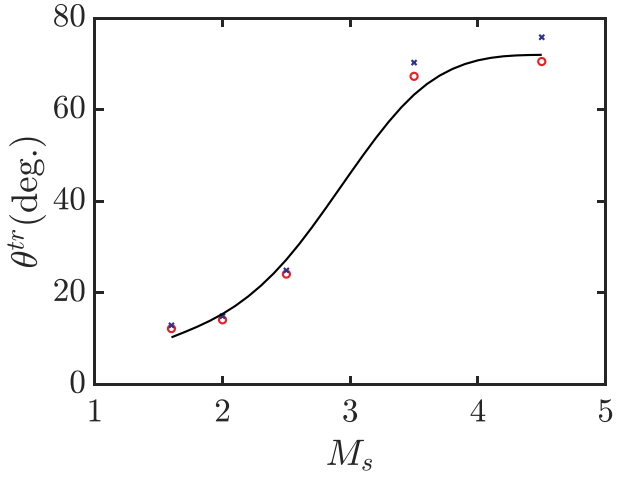

Fig. 4. Transition angles from regular to Mach reflection (RR → MR), over: ◦ the first concave surface; × the second concave surface; - fitting curve, *vs*. Incident-shock-wave Mach numbers.

$M_s = 1.6$. It can be seen that the two parameters start to be mesh independent from $\mathscr{G}_3$. Based on these observations a mesh resolution of $\mathscr{G}_4$ is used for the rest of the study.

Fig. 4 shows the RR → MR transition angles, θ^{tr}, over the first and the second concave surfaces. As it can be seen, θ^{tr} increases for larger shock-wave Mach numbers M_s. It is also interesting to note that θ^{tr} is almost the same for both surfaces, except for $M_s = 3.5$ and 4.5 in which θ^{tr} is relatively larger on the second surface (approximately 7% for $M_s = 4.5$ and 4% for $M_s = 3.5$). Soni et al. in their study [13] found θ^{tr} to be larger on the second cylindrical reflector (for Mach numbers up to $M_s = 2.5$) and they noted that this behavior can be perceived as resulting from the fact that the flow regions behind the Mach stems are subsonic, hence the information can be communicated through them.

In order to track the triple points, the ℓ^2- norm of the pressure gradient is computed, which translates to the analytical formula for the two-dimensional case at the *n*th time step as;

$$TP^n = \sqrt{\left(\frac{\partial p}{\partial x}\right)_n^2 + \left(\frac{\partial p}{\partial y}\right)_n^2} \tag{8}$$

Applying max (TP^n, TP^{n-1}) for each time step would give the entire trajectories of the triple points[13]. Figs. 5 and 6 show the shock reflection process on the second concave, for the Mach numbers: 3.5 and 4.5 respectively . In Figs. 5(a) and 6(a) we can see the presence of a single triple point (TP_2), this configuration is known as a STP (single triple point) configuration. A little further a second triple point is formed (TP_3 in Fig. 5(b) and 6(b)). This makes a transition from a

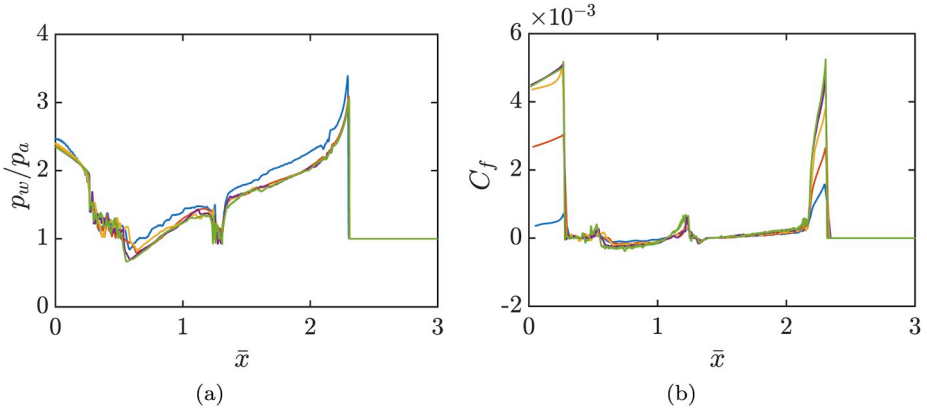

Fig. 3. (a): Non-dimensional wall-pressure distribution, (b): skin friction distribution at t = 294 μs for different grid resolutions at $M_s = 1.6$ ($\mathscr{G}_0$, $\mathscr{G}_1$, $\mathscr{G}_2$, $\mathscr{G}_3$, $\mathscr{G}_4$).

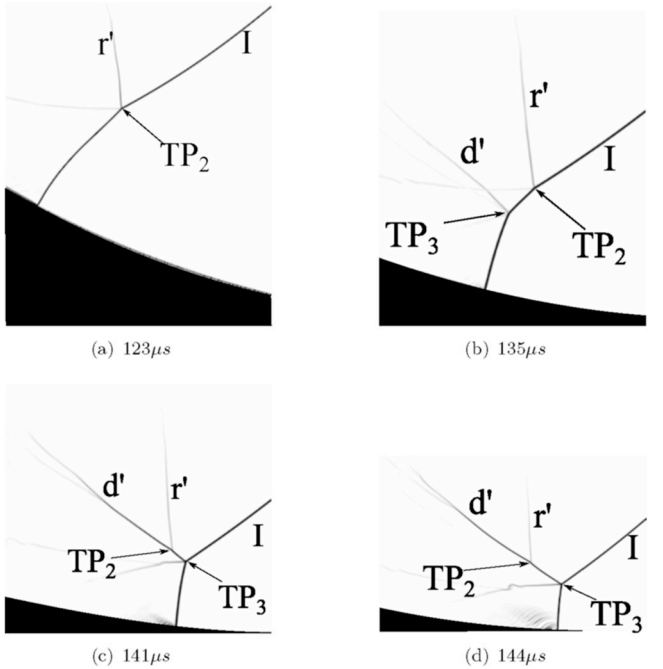

Fig. 5. Numerical schlieren pictures for $M_s = 3.5$ for the second concave surface, at different instant. r' and d': reflected and additional shocks created on the second concave surface, respectively, I: incident shock, TP: triple point.

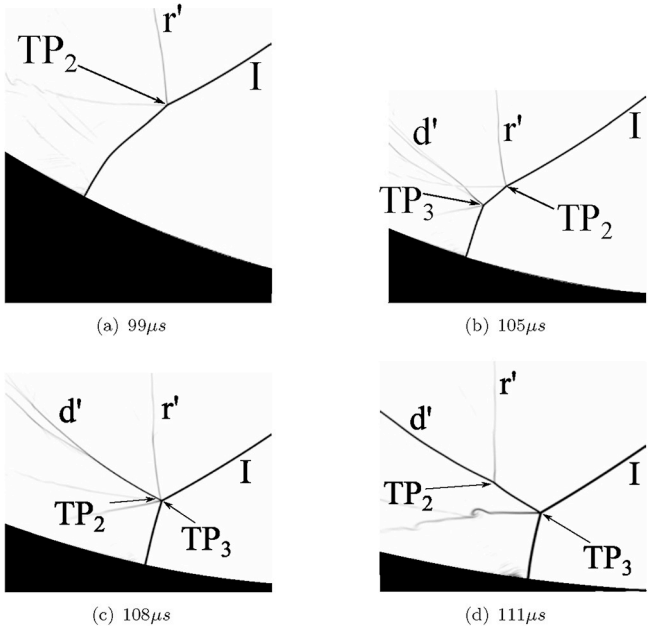

Fig. 6. Numerical schlieren pictures for $M_s = 4.5$ for the second concave surface at different instant. For legend, see caption of Fig. 5.

single-TP configuration to a double-TP configuration (STP → DTP transition) . Fig. 7 depicts the Triple Points trajectories obtained for the five shock-wave Mach numbers used in this study $M_s = 1.6$; $M_s = 2.5$; $M_s = 3.5$ and $M_s = 4.5$ (result for $M_s = 2.0$ is not shown as it is almost identical to that of $M_s = 2.5$). For the first surface and for the relatively low shock-wave Mach number ($M_s = 1.6$; 2.5) (Fig. 7(a) and (b)), a Mach reflection at the end of the surface is observed with a weak reflected shock-wave. For the higher mach numbers ($M_s = 3.5$; 4.5) (Fig. 7(c) and (d)) we observe a regular reflection (RR) just at the beginning of the surface, a little further on, a transition to a Mach reflection (MR) (RR → MR) takes place to give rise to a Mach reflection with stronger reflected shock-waves. For the second surface there is a change in behavior for the two shock-wave Mach numbers; $M_s = 3.5$ and 4.5 while for the shock-wave Mach numbers; $M_s = 1.6$, 2.0 and 2.5 the behavior of the shock-wave remains the same as that of the first surface. For the shock-wave Mach number $M_s = 1.6$, 2.0 and 2.5, we notice the apparition of a Mach reflection (MR) at the end of the surface. By increasing the shock-wave Mach number to 3.5 and 4.5, (Fig. 7(c) and (d)) the behavior is completely different. At the beginning of the second surface, we notice the appearance of a regular reflection (RR) followed by a transition to a Mach reflection (MR) (RR → MR), characterized by the formation of a triple point (it is a STP configuration). Further, at the end of the surface, we notice the appearance of a second triple point (which is a DTP configuration) appearing in this case. This makes a transition from a STP to a DTP configuration. For $M_s = 4.5$ and as the shock-wave moves further up, the two triple points merge together to give birth to a single-TP configuration again. So, we have STP → DTP → STP configuration. Another point to note is that the Mach stem associated with TP_3 for the $M_s = 4.5$ is more substantial than the one seen for $M_s = 3.5$.

4.2. Shock-wave propagation and its attenuation

Here we present the possible influence of grid resolution on the shock front position and velocity by using different meshes. We compared the values of $\bar{x}_s$ and W_s/W_s^i (where W_s is the velocity of the incident shock and W_s^i is the initial velocity of the incident shock) obtained by using five different refinements, and found their difference to be negligible (see Fig. 8(a) and (b) respectively). This indicates that the obtained solution is mesh independent. Fig. 8(a) shows the time evolution of the transmitted shock wave. After an initial linear evolution, the evolution of the transmitted shock wave becomes non-linear the velocity of the transmitted shock wave decreased as can be seen in Fig. 8(b), where, in the beginning before reaching the corner, the transmitted shock-wave moves with a constant velocity (equal to the initial velocity (W_s^i), the value given by the shock-tube theory (black line in Fig. 8(b), $W_s/W_s^i = 1$)). Once the shock-wave reaches the corner of the double concave, its velocity starts to decrease due to the deceleration of the transmitted shock-wave.

We will now discuss the evolution (speed and position) of the shock wave propagating within the double concave surfaces, by changing the incident shock-wave Mach number M_s and using the mesh resolution $\mathscr{G}_4$. Fig. 9(a) illustrates the evolution of the incident shock wave location ($\overline{x_s}$) as a function of dimensionless time ($\bar{t}$). By differentiating x_s with respect to t, one can easily obtain the dimensionless velocity (W_s/W_s^i) of the shock (Fig. 9(b)), for all shock-waves strength, the speed of the incident shock wave starts with a constant value (equal to the initial velocity) ($W_s/W_s^i = 1$), and decreases steadily in time. Furthermore, its rate of change is at first very large, but becomes smaller as it propagates through the double concave surfaces, and as we can see in Fig. 9(b), the speed of the incident shock wave starts to decrease earlier for stronger shock waves (highest shock-waves Mach numbers) and this result is expected because the shock waves with high shock-wave Mach numbers reach the corner of the double concave first, and the velocity deficit is increasing with the shock-wave Mach number.

The shock trajectory and velocity are plotted using dimensionless coordinates. By finding the appropriate dimensionless time, it was possible to show the data from different simulations with different Mach numbers collapse into a single curve. From the data analysis, the following relationship is found:

$$\tilde{t} = \frac{W_s^i}{R}\phi(\gamma, M_s)\, t \tag{9}$$

The scaling function $\phi(\gamma, M_s)$ is defined as:

$$\phi(\gamma, M_s) = (M_s + 1)\, ln(M_s + 1)^{1/\gamma} - \frac{\gamma - 1}{\gamma}(M_s^2 - 1) \tag{10}$$

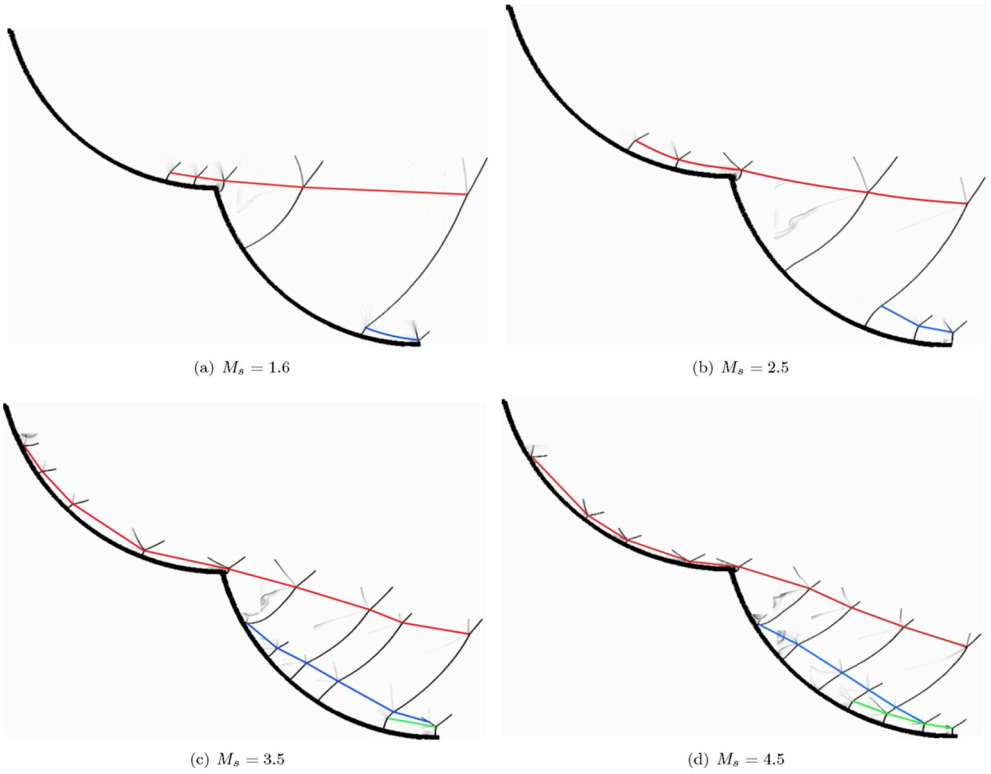

Fig. 7. Trajectories of the triple points for different shock-wave Mach numbers: (a): $M_s = 1.6$; (b): $M_s = 2.5$; (c): $M_s = 3.5$; (d): $M_s = 4.5$; (—: TP_1; —: TP_2; —: TP_3).

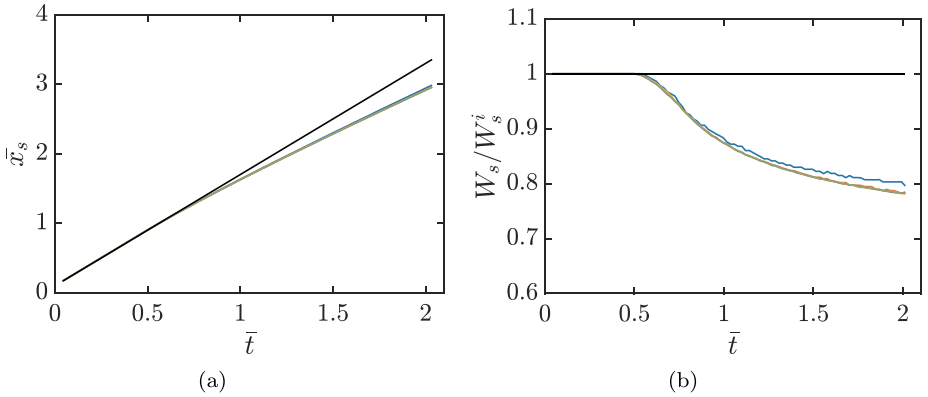

Fig. 8. Non-dimensional; (a); shock position and (b); shock velocity for different mesh resolutions; (– $\mathscr{G}_0$, – $\mathscr{G}_1$, – $\mathscr{G}_2$, – $\mathscr{G}_3$, – $\mathscr{G}_4$, — shock position and velocity given by the piston theory).

By applying this normalization (Equation (9)), all results (shock position, shock velocity for different Mach numbers) collapse together into single curve and the results are presented in Fig. 9(c) and (d) respectively.

5. Summary

In this paper, shock-waves diffraction over double-cylindrical wedges (the centre of the first concave surface is at higher y-cordinate than the second one) have been investigated. Numerical simulations were carried out to study the dynamics of shock wave with regards to the incident-shock-wave Mach number. Different grid resolutions were used to investigate the grid size effect on the numerical solutions and it was found that the quantities studied (transition angle, pressure and skin friction distributions at the wall, shock position and velocity) are mesh independent from certain resolution ($\Delta x_{min} = 20\mu m$, $\Delta y_{min} = 21\mu m$). The transition angle increases with Mach number, and was found to be almost the same over the two concave surfaces for weak Mach numbers (up to $M_s = 2.5$) and to be relatively larger on the second surface for high Mach numbers (approximately 7% for $M_s = 4.5$, 4% for $M_s = 3.5$), the behavior of the shock wave is completely different for $M_s = 4.5$, at the end of the second concave surface we have a STP→DTP→STP configuration, indicating that the flow was capable of retaining the memory of the past events over the entire process for high Mach numbers. In terms of shock's velocity, the velocity deficit was found to be increasing with Mach number. The shock position and shock velocity are proportional to the shock initial velocity reduced by a scaling function that depending on the incident shock-wave Mach number, the heat capacity ratio and the concave surface radius. The proposed scaling was tested in the range of M_s ($1.6 < M_s < 4.5$), for heat ratio of 1.4 and concave surface radius of $50mm$.

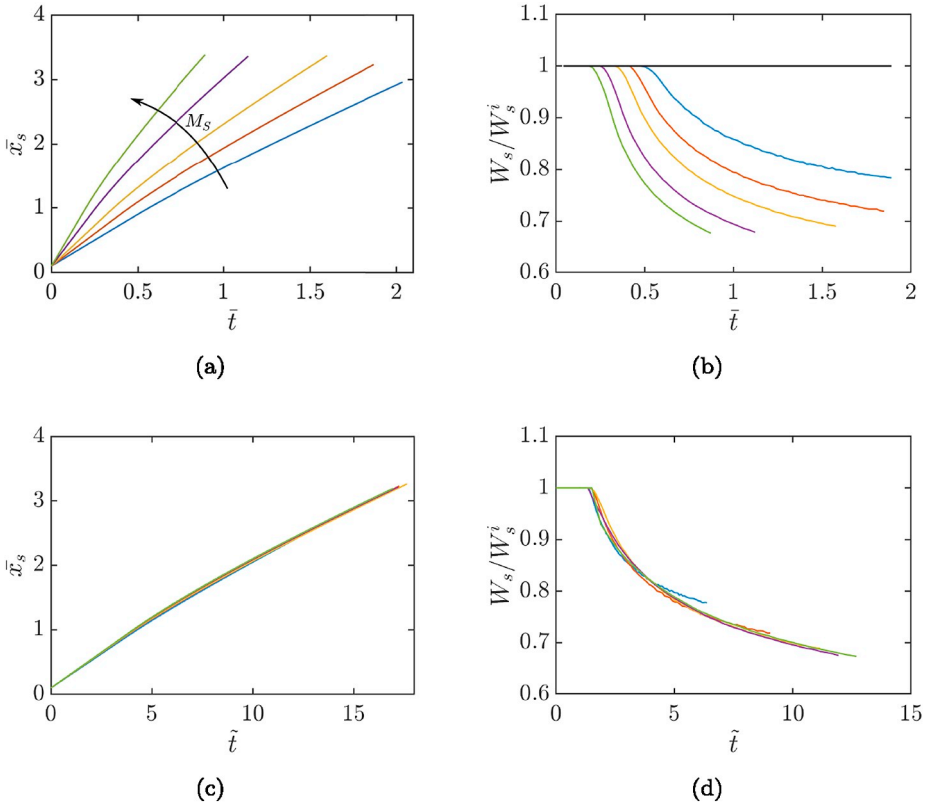

Fig. 9. Normalized; (a): shock-wave position; (b): shock-wave velocity; (c): Normalized shock-wave position *vs*. normalized time and (d): normalized shock-wave velocity *vs*. normalized time, for different shock-wave Mach numbers ($M_s = 1.6$, $M_s = 2.0$, $M_s = 2.5$, $M_s = 3.5$, $M_s = 4.5$, shock velocity given by the piston theory).

Acknowledgments

N. Brahmi gratefully acknowledges support from the Algerian Government through a PHD Fellowship. Computational facilities from 'Centre Régional Informatique et d'Applications Numériques de Normandie (CRIANN)', Rouen, France under allocation 1998022, are acknowledged.

References

[1] G.B. Whitham, On the propagation of weak shock waves, J. Fluid Mech. 1 (3) (1956) 290–318.
[2] G.B. Whitham, A new approach to problems of shock dynamics part i two-dimensional problems, J. Fluid Mech. 2 (1957) 145–171.
[3] G.B. Whitham, On the propagation of shock waves through regions of non-uniform area or flow, J. Fluid Mech. 4 (1958) 337–360.
[4] G.A. Bird, The effect of wall shape on the degree of reinforcement of a shock wave moving into a converging channel, J. Fluid Mech. 5 (1959) 60–66.
[5] T.V. Bazhenova, L.G. Gvosdeva, Y.V. Zhilin, Change in the shape of the diffracting shock wave at a convex corner, Acta Astronaut. 6 (1951) (1979) 401–412.
[6] L.F. Henderson, On the whitham theory of shock-wave diffraction at concave corners, J. Fluid Mech. 99 (4) (1980) 801–811.
[7] R. Hillier, Computation of shock wave diffraction at a ninety degrees convex edge, Shock Waves 1 (2) (1991) 89–98.
[8] S. Sivier, E. Loth, J. Baum, R. Löhner, Vorticity produced by shock wave diffraction, Shock Waves 2 (1) (1992) 31–41.
[9] B. Skews, A. Blitterswijk, Shock wave reflection off coupled surfaces, Shock Waves 21 (6) (2011) 491.
[10] A.E. Bryson, R.W.F. Gross, Diffraction of strong shocks by cones, cylinders, and spheres, J. Fluid Mech. 10 (1) (1961) 1–16.
[11] L.F. Henderson, A. Lozzi, Experiments on transition of mach reflexion, J. Fluid Mech. 68 (1) (1975) 139–155.
[12] I.V. Krassovskaya, M.K. Berezkina, Mechanism of formation of reflection configurations over concave surfaces, Shock Waves 27 (3) (2017) 431–439.
[13] V. Soni, A. Hadjadj, A. Chaudhuri, G. Ben-Dor, Shock-wave reflections over double-concave cylindrical reflectors, J. Fluid Mech. 813 (2017) 70–84.
[14] M.V. Chernyshov, O.A. Tolpegin, Optimal regular reflection of oblique shocks, Acta Astronaut. (2019) 1–7, https://doi.org/10.1016/j.actaastro.2019.01.015.
[15] L. Gvozdeva, M. Silnikov, S. Gavrenkov, Triple shock configurations with negative angle of reflection, Acta Astronaut. 116 (2015) 36–42.
[16] N.N. Smirnov, O.G. Penyazkov, K.L. Sevrouk, V.F. Nikitin, L.I. Stamov, Onset of detonation in hydrogen-air mixtures due to shock wave reflection inside a combustion chamber, Acta Astronaut. 149 (2018) 77–92.
[17] N.N. Smirnov, O.G. Penyazkov, K.L. Sevrouk, V.F. Nikitin, L. Stamov, V. Tyurenkova, Detonation onset following shock wave focusing, Acta Astronaut. 135 (2017) 114–130.
[18] V. Soni, Parallel Adaptive Multiscale Numerical Methods for Complex Compressible Flows, PHD Thesis, INSA Rouen, FRANCE, 2016.
[19] V. Soni, A. Hadjadj, O. Roussel, On the use of adaptive multiresolution method with time-varying tolerance for compressible fluid flows, Shock Waves (2017) 1–14.
[20] V. Soni, A. Hadjadj, O. Roussel, G. Moebs, Parallel multi-core and multi-processor methods on point-value multiresolution algorithms for hyperbolic conservation laws, J. Parallel Distr. Comput. 123 (2019) 192–203.
[21] A. Chaudhuri, A. Hadjadj, A. Chinnayya, On the use of immersed boundary methods for shock/obstacle interactions, J. Comput. Phys. 230 (5) (2011) 1731–1748.
[22] A. Chaudhuri, A. Hadjadj, A. Chinnayya, S. Palerm, Numerical study of compressible mixing layers using high-order WENO schemes, J. Sci. Comput. 47 (2) (2011) 170–197.
[23] M. Berezkina, I.V. Krasovskaya, D.Kh. Ofengeim, Diffraction of a Two-Shock Configuration by a Convex Cylindrical Surface, Technical Physics 51 (2006) 827–833.
[24] M. Berezkina, I.V. Krasovskaya, D.Kh. Ofengeim, Diffraction of a Two-Shock Configuration by a Concave Cylindrical Surface. Technical Physics 52 (2007) 1271–1280.